

Highly ordered LIPSS on Au thin film for plasmonic sensing fabricated by double femtosecond pulses

Fotis Fraggelakis^{1,*}, Panagiotis Lingos¹, Emma Cusworth², Vasyl G. Kravets², Alexander N. Grigorenko²,
Andrei V. Kabashin³ and Emmanuel Stratakis^{1,4*}

¹Institute of Electronic Structure and Laser (IESL), Foundation for Research and Technology (FORTH), N. Plastira 100, Vassilika Vouton, 70013 Heraklion, Crete, Greece

²Department of Physics and Astronomy, Manchester University, Manchester M13 9PL, UK

³Aix Marseille Univ, CNRS, LP3, Campus de Luminy, Case 917, 13288, Marseille, France

⁴Department of Physics, University of Crete, 71003 Heraklion, Crete, Greece

*Correspondence: fraggelakis@iesl.forth.gr, stratak@iesl.forth.gr

Abstract

We report on the single-step fabrication of homogeneous and highly ordered Laser Induced Periodic Surface Structures (LIPSS) over large areas on Au nanolayers, that can be used for plasmonic sensing. A comprehensive study on LIPSS formation on 32 nm Au film upon double, 170 fs pulse irradiation, unveiled the key importance of interpulse delay as the determining factor behind the homogeneity of laser induced structures and confirmed that highly ordered, functional LIPSS occur solely upon double pulse irradiation. In particular, the impact of pulse overlap, fluence and interpulse delay reveals that homogeneous LIPSS formation is optimized within a specific interpulse delay range. At the same time, examination of nanoscale features of the structures points out a significant differentiation of the LIPSS formation characteristics between single and double pulse irradiation. Theoretical investigation complements experimental results providing insights on the structure formation mechanism. Ellipsometric measurements validate that such structures exhibit characteristic plasmon resonances that can be exploited for sensing applications. The presented data demonstrate a novel functionality of LIPSS, while providing strong evidence of the capabilities of femtosecond double pulse irradiation as a valuable and low-cost tool for the precise fabrication of highly ordered structures.

1. Introduction

Laser surface processing is emerging as an efficient way to transform the properties of solid surfaces. Micro and nano morphologies, often inspired by nature, have been fabricated by laser on various materials to artificially tailor surface properties¹. Among the functionalities reported for bulk materials are coloring², superhydrophobicity³, anti-icing⁴, anti-reflectivity⁵, surface blackening⁶ altered bacteria⁷ and cell adhesion⁸. Currently, the scientific interest for laser surface processing of materials with thickness in the order of the optical penetration depth, so called thin films, is increasing rapidly⁹. Structures developed on thin films can be used in various applications including optical elements¹⁰, plasmonic sensors⁹ and substrates for nanomaterial growth^{11,12}. Fabricating surface structures via laser, offers many advantages compared to other techniques such as photolithography or e-beam lithography. In particular, it is a cheap, fast, scalable and chemical free process. Furthermore, the constant increase of laser processing throughput and the speed of positioning systems enable laser surface processing be a viable industrial scale solution for materials' functionalization.

Nature provides a variety of functional surfaces from which the laser engineering of biomimetic surfaces field is inspired¹⁻¹³. The eventual functionality attained upon laser processing is the collective result of the surface morphology at the both the micro- and the nano-scale level¹² with the reported features covering a broad palette of shapes, sizes and hierarchical formation¹. In this context, reproducing functionalities found in nature on technical surfaces is always coming down to controlling the laser-induced morphology and numerous studies have been focused in developing new structures^{14,15} or in tailoring structures geometry¹⁶. The most common type of laser-induced structure that can be fabricated in almost any kind of material is LIPSS, Particularly, the Low Spatial Frequency LIPSS (LSFL)¹⁷ are periodic structures with sizes in the range of laser wavelength and can have either uniaxial (1D-LIPSS) or multiaxial symmetry (2D-LIPSS). LIPSS with periodicities well below the laser wavelength ($\lambda/2$ to $\lambda/10$) are coined as high spatial frequency LIPSS (HSFL)¹⁷.

Key process parameters such as laser wavelength, polarization, fluence and number of incident pulses can have a major impact on LIPSS formation. In particular, the LSFL period is linked to the laser wavelength, whereas the HSFL period seem to depend mostly on other parameters, such as the laser fluence and the pulse duration¹⁸. At the same time, the final structure formation is a multi-pulse process where the surface relief is shaped progressively pulse after pulse¹⁹, therefore a certain number of pulses is required for developing pronounced structures. When large areas are textured, the delivery of evenly distributed amounts of energy over the processed area is essential to maintain the homogeneity of the structures formed, which makes the irradiation strategy a crucial aspect of the process. More complex morphologies arise when pulse characteristics such as polarization, spatial intensity and temporal profile are tailored. For example 2D-LIPSS can be fabricated upon irradiation by beams with circular²⁰ and azimuthal/radial polarization²¹.

Understanding the underlying structure formation mechanism is essential to control the laser-induced surface morphology. Even though there is no generally accepted model, LIPSS are considered to be the result of the synergistic contribution of two processes; Inhomogeneous light absorption which occurs during the irradiation (Process I) and thermal and hydrodynamic which take place at timescales much longer than the pulse duration (Process II)^{14,19,22,23}. The different timescales of the two processes were unveiled by both pump-probe experiments^{24,25} and simulations²⁶.

In a descriptive view, Process I refers to the setting of the initial conditions of the surface reorganization process. Mainly, pulse polarization, energy and intensity distribution as well as the material's electronic structure and surface morphology define the distribution of the energy on the surface during irradiation. There are plenty of theoretical and experimental works which attribute the origin of laser-induced nanoscale periodic structures on metallic surfaces to the superposition of the incident laser beam with the scattered electromagnetic waves such as surface plasmon polaritons (SPPs) created on the air-metal interface and evanescent quasi-cylindrical waves²⁷⁻³⁰. SPPs are considered the dominant source of surface waves, a process that results from the coherent interaction of the incident laser field with free electrons created in the material³¹. According to that model, polarization control and spatial beam shaping are expected to have a major impact on Process I by imposing the absorption pattern. Following the equilibration between electrons and lattice and depending on the deposited energy, the material surface melts or ablates and ultimately resolidifies in nanosecond timescales³². Considering sub ablation conditions, the temperature gradients residue from Process I¹⁹ give rise to surface tension and molten materials' density variations along the surface that drive the displacement of molten material due to hydrodynamical motion¹⁹. Depending on the amplitude and the steepness of the temperature gradient,

different hydrodynamical effects may take place including Marangoni flow^{19,33}. Heat is gradually dissipated into the bulk, the melting depth and temperature changes affecting the hydrodynamical values of the process such as materials viscosity, density and thermal conductivity. Several aspects of this dynamic process are yet to be unveiled and can only be fully understood via multiscale simulation. Recently the role of pressure waves in the development of flow instabilities was investigated theoretically³³.

Both Processes I and II can be tailored to some extent upon double pulse irradiation (DPI) via the variation of the interpulse delay separation time, $\Delta\tau$, and the polarization state. In particular, it has been shown that DPI with interpulse delay time in the picosecond regime can have a strong impact on the morphology attained, enabling control over the hierarchical formation of 2D-LIPSS¹⁴. Moreover, DPI can be employed to increase structure homogeneity over large area, producing highly ordered structures^{34,35}. DPI in picosecond delay times is also linked to the HSFL formation, as hierarchical 2D-LIPSS and HSFL^{14,36}, as well as homogeneous nanoholes and nano protrusions^{34,37,38}. DPI is also expected to have a drastic impact on Process II^{39,40}, considering that case the second pulse arrives at the surface during the evolution of the hydrodynamical phenomena²⁶. When DPI is combined with spatial pulse shaping, for example upon using Direct Light Interference Patterning control over both Process I and II can be realized³⁹, giving rise to the generation of structures⁴⁰.

Although the aforementioned mechanisms are mostly applicable for bulk materials, some of the basic principles of LIPSS formation can be also applicable to the case of thin metallic films with thickness in the order of a few tens of nanometers. Nonetheless, significant differences are anticipated⁴¹, considering that the material's thickness is comparable with the penetration depth of the laser radiation. In particular, metallic thin films are embedded on two dielectric media, the superstrate (i.e. air) and the substrate, exhibiting two interfaces where SPPs could be simultaneously excited. When the film thickness is comparable to the penetration depth, the SPP mode on the one interface can transfer energy to the other through the film and vice versa which results in complex spatial modulation and distribution of the laser energy within the material^{42,43}. Moreover, during LIPSS formation the pulse energy and the total number of pulses should be properly controlled to avoid film damage⁴¹. Finally, the development of plasmonic devices are mostly based on noble metals, in which LIPSS are hard to form upon single pulse irradiation⁴⁴.

In this work we employ DPI to overcome the above-mentioned limitations related to thin film laser processing of noble metals and fabricate homogeneous LIPSS on 32nm Au thin film. Both ps and ns interpulse delay regimes are investigated, while the impact of important process parameters such as pulse to pulse overlap and laser fluence is carried out. Besides this, the role of $\Delta\tau$ in the homogeneity of the structures attained is thoroughly investigated and discussed. As determined by spectroscopic ellipsometry measurements, the fabricated LIPSS structures exhibit pronounced plasmon resonances, making such structures suitable for sensing applications.

II. Experimental part

a) laser processing

Thin Au films with thickness of $d_{Au}=32 \pm 2$ nm on glass substrate ($d_{Sub}=170 \mu\text{m}$) have been laser processed using the radiation of a 170 fs laser source emitting at 1030 nm (Light Conversion, Pharos). For the

generation of the double pulses and the tuning of $\Delta\tau$ a setup shown in Figure 1 was developed. In detail, the main beam is divided into two parts by a polarizing beam splitter (BS) and then is guided into two arms, Arm A and Arm B respectively. Arm A is controlled by a computer-assisted micrometer displacement controller (DC) used for setting the $\Delta\tau$ value in the range of 0 to 50 ps with accuracy of 2 fs. Arm B is placed on a manual dovetail rail to produce $\Delta\tau$ values in the range of 100 ps to 2 ns with an accuracy of ~ 3.5 ps.

The first half wave plate ($\lambda/2$) combined with a linear polarizing cube (LPC) is utilized to control the fluence distribution between the two pulses. The second $\lambda/2$, in Arm B, controls the polarization of Arm B, which in this series of experiments is fixed vertically as shown in Figure 1. As a result, the two arms generate two pulses with parallel polarization onto the sample surface. The recombination of the beams of the two arms in colinear propagation is realized by the BS. Beam attenuation is realized via a computer controlled $\lambda/2$ in combination with a LPC. A computer-controlled attenuation part consisting of a half waveplate and a LPC is used to tune the pulse energy. A polarization control unit consisting of a $\lambda/2$ is used to control the polarization direction onto the sample plane. The sample is placed on a programmable 3-axis motorized stage. The spot size $2w_0$ was calculated to be ~ 55 μm in diameter at $1/e^2$ using a CCD camera placed at the focal plane. The overlap of the two pulses is estimated with accuracy in the order of the pulse duration (170 fs), utilizing a second harmonic generation (SHG) crystal. The experiments were conducted at normal incidence and in ambient air. The process parameters considered in the experimental part are: The average fluence, Φ that is calculated using the equation (1) in Table 1 where the E_p is the energy per pulse measured with a pyroelectric power meter. The overlap (Ov) is estimated as the average number of incident pulses at any point of irradiated area (pps) as describe in the equation (2) of Table 1, where u is the average speed and f the repetition rate. Finally, $\Delta\tau$ is calculated using equation (3) of Table 1, where c stands for the speed of light, ΔL is the optical path difference of the two beams while the presence of the factor of 2 comes from the fact that the pulse travels two times the displacement of the arm due to the setup geometry. The hatch, H is defined as the step between the scanning lines and is fixed to $H = 2$ μm , after some preliminary study, unless otherwise stated. Finally, the average dose $D = \Phi \cdot pps$ is a measure of the total irradiation energy per spot.

Table 1:1 Process parameters and value ranges

| Value | Symbol | Equation | Min | Max |
|------------------|--------------|---|--|------------------------|
| Fluence | Φ | (1) $\Phi [J/cm^2] = E_p / \pi w_0^2$ | 0.04 J/cm ² | 0.16 J/cm ² |
| Overlap | Ov | (2) $Ov [pps] = (2w_0/u) \cdot f$ | 20 pps | 400 pps |
| Hatch | H | | 2 μm | 20 μm |
| Interpulse delay | $\Delta\tau$ | (3) $\Delta\tau (ps) = 2 \cdot \frac{\Delta L (\mu m)}{c} \cdot 10^6$ | 0 ps, 5 ps, 10 ps, 20 ps, 50 ps, 100 ps, 300 ps, 500 ps, 800 ps, 1 ns, 1.5 ns, 2 ns. | |

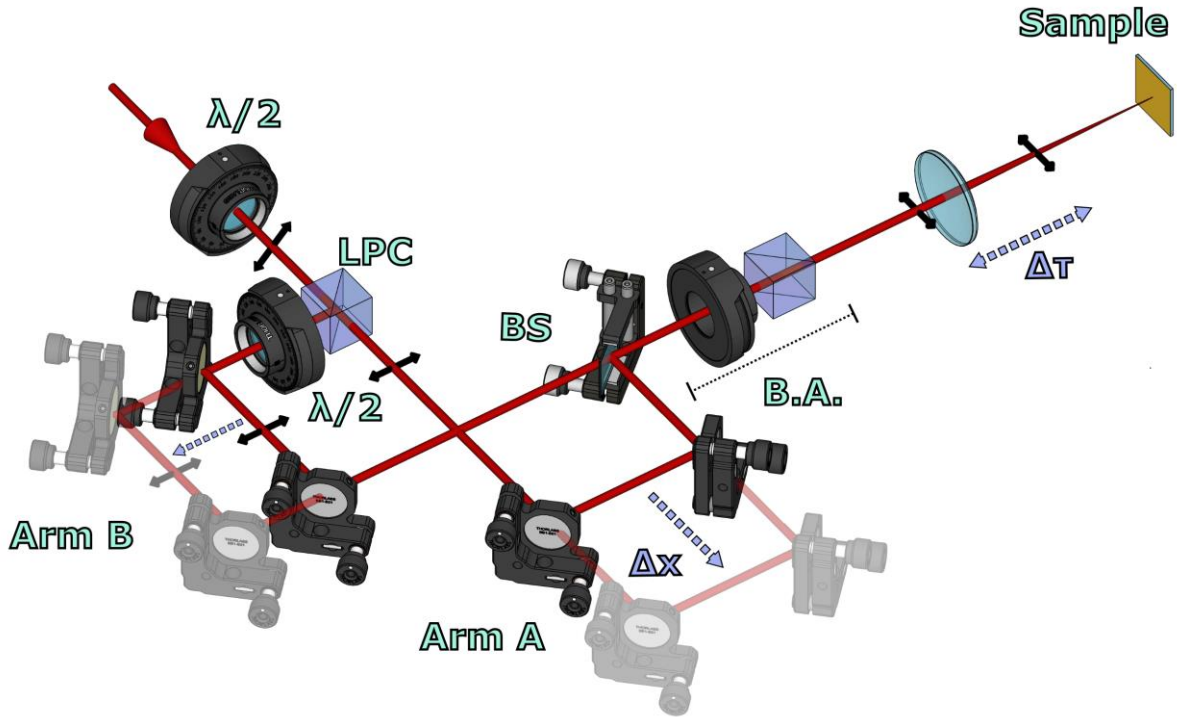


Figure 1. The setup. Abbreviations: beam splitter (BS), linear polarizer (LPC), half waveplate ($\lambda/2$), Attenuation part (AT), polarization control part (PC). Linear displacement (Δx), time delay (Δt).

The morphologies of the laser-fabricated structures were visualized by a field-emission Scanning Electron Microscope (SEM). All the measurements of the features of surface structures were performed by a 2D-FFT analysis of the corresponding SEM images using Gwyddion (<http://gwyddion.net/>), a free and open-source software for data visualization and analysis.

b) Electromagnetic Simulations

Here we provide a description of the theoretical model used for the determination of the electromagnetic modes that are excited after irradiation of a thin Au film with fs pulses. Analytical approaches such as the Sipe theory, provides a *near-surface* description of the inhomogeneous absorption of optical radiation by the roughened surface⁴⁵. On the other hand, computational approaches based on the numerical solution of the Maxwell equations such as finite-difference time-domain (FDTD)⁴⁶ and finite integration technique (FIT)⁴⁷ are capable to provide details about the electromagnetic modes produced on complex media in three dimensions. We investigate numerically the spatial modulation of the energy below the irradiated rough surface of a $d = 32$ nm thick Au/SiO₂ thin film, resulting from the electromagnetic field distribution i.e. SPP coupling between the two dielectric-metal interfaces and other surface waves, by solving the integral form of the Maxwell equations. For this purpose, the Maxwell's Grid Equations are solved considering a three layer system (air-metal-glass) with optical constants $\epsilon_a = 1$ (air), $\epsilon_g = 2.1$ (glass) and $\epsilon_m = -44.47 + i3.2$ (Au)⁴⁸ for laser wavelength $\lambda_L = 1026$ nm. For Au thin film described above, the optical skin depth is comparable to the film thickness. The laser beam is considered to be a normally-incident plane-wave and linearly polarized along the x -axis of duration $t = 100$ fs. The laser beam is propagating along the z axis and the xy plane, i.e. the sample plane, is perpendicular to the propagation

direction. We keep simple periodic boundary conditions for xy , while at the z -boundaries normal to the propagation, convolutional perfectly matched layers (CPML) are used in order to truncate the computational domain and avoid non-physical reflections at the edges of the simulation grid. The periodic effects due to periodic boundary conditions are of low importance since the irradiated metallic area is large enough and can be suppressed by the optical losses. Using the boundary conditions described above, the spatial laser profile matches perfectly the xy plane of the structure with homogeneous intensity distribution. The surface roughness plays the key role in electromagnetic wave scattering and generation of SPP that are the precursors of LIPSS. To emulate the features of a rough surface, we introduce randomly distributed scattering centres in the form of nano-holes of radius $r < d$ along the film surface. The concentration of inhomogeneities at the air/Au interface is considered to be $C = N\pi r^2/S \approx 0.25\%$ where N is the number of the nano-holes and the laser affected area $S = 10 \times 10 \mu\text{m}^2$. A similar approach has been introduced in similar studies for bulk materials^{29,49,50}. The interaction of light with the surface inhomogeneities of the material produces electromagnetic interference patterns along the surface, which determine the energy absorption landscape. Since the absorbed energy of the film is proportional to the intensity, in order to capture the absorption energy maxima and minima due to scattering of overlapping surface waves, we calculate the normalized intensity difference $(I - I_S)/I_S$ where $I \sim |\vec{E}|^2$ is total intensity of Au films below the rough surface, while I_S is the total intensity of Au below a defect-free surface. This difference depicts the intensity maxima and minima due to both scattered radiative and non-radiative fields by the subwavelength imperfections.

c) Ellipsometric Measurements

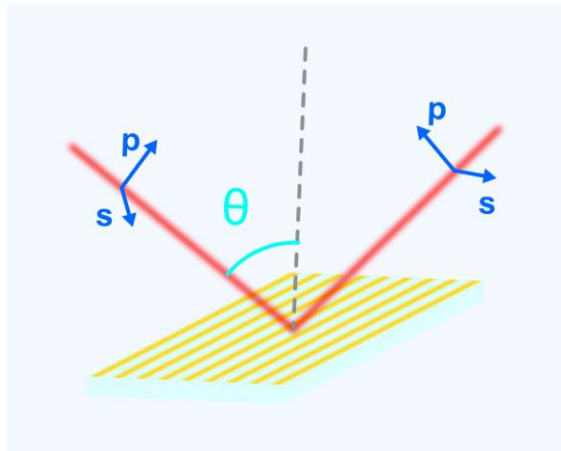


Figure 2 Schematic diagram of ellipsometric measurement for gold patterned nanostructures and geometry of orientation of ablated samples with respect to the direction of incident polarised light.

To measure optical properties of the fabricated samples, we used a variable angle focused-beam spectroscopic ellipsometer Woollam M 2000F. It is based on the rotating polariser-compensator-analyser setup (Figure 2) and utilises a diode array spectrophotometer to extract the spectral parameters Ψ (ellipsometric reflection) and Δ (ellipsometric phase) in the wavelength range of 240-1690 nm, with a wavelength step of ~ 1.0 nm for 240-1000 nm and ~ 2.0 nm for 1000-1690 nm. The beam spot size on the sample was approximately $30 \mu\text{m} \times 60 \mu\text{m}$ for $\sim 60-70^\circ$ angles of incidence. These parameters are related to the sample reflection as $\tan(\Psi) \exp(i\Delta) = r_p/r_s$, where r_p and r_s are the amplitude reflection coefficients for p - and s -polarized light, respectively. In addition to ellipsometric parameters Ψ and Δ , the ellipsometer enables one to separately measure $R_p = |r_p|^2$ and $R_s = |r_s|^2$ providing the intensity reflection spectra for p - and s -polarised light,

respectively. The errors on the polariser, compensator and analyser azimuthal parameters are generally less than $\pm 0.01^\circ$, which implies that, the ellipsometric parameters Ψ and Δ can be measured with an error of level $\pm 0.02^\circ$. The schematic for ellipsometry measurements is presented in 2, showing that the Au plasmonic LIPSS were oriented in such a way that the plane of incidence was parallel to the array lattice vector (i.e the LIPSS were perpendicular to the plane of incidence). An Ultra Plus Carl ZEISS SEM was used

for high-resolution imaging of the nanostructures. The unique in-lens SEM detector gives resolution of the order of 1.0 nm at 15 kV (1.6 nm at 1 kV), dependent on the type of samples.

Theoretical modelling of optical properties of fabricated samples was performed with the help of Fresnel theory where we applied the effective-medium approximation (EMA) to the top metal layer nanostructured by laser ablation. WVASE32 software of J.A. Woollam Company was used to perform calculations. The model geometry for studied samples was chosen to be constructed of three layers: glass as a substrate, unperturbed film of Au and an EMA layer of ablated gold film which was a combination of gold and air. The optical constants of EMA layer were calculated using a Maxwell-Garnett theory. The thickness of the unperturbed gold layer, thickness of the EMA layer and the ratio of void to gold in the EMA layer were varied to achieve the best fit with the measured data.

III. Results and discussion

In this part the morphology obtained following double pulse laser irradiation of Au thin films is presented and discussed. The laser processing results are complemented with theoretical simulations on laser surface coupling and surface functionality characterization.

a) Resulting morphology for single and double pulse irradiation

Figure 3 illustrates the resulting morphology on Au surface after irradiation with single and double pulses respectively. The overlap value is fixed for all cases to $O_v = 150$ pps, whereas the fluence and $\Delta\tau$ values vary as indicated. Different fluence ranges are considered for single and double pulses; For single pulses the fluence values varies between $\Phi = 70$ and $100 \mu\text{J}/\text{cm}^2$, while for double pulses between $\Phi = 80$ and $120 \mu\text{J}/\text{cm}^2$. The fluence values are chosen appropriately to illustrate the different laser induced morphologies from structure appearance (low Φ) to thin film damage (high Φ). The difference in the Φ values between single and double pulses is attributed to the variation of the effective fluence between single and double pulses irradiation as well as between different $\Delta\tau$ values⁵¹.

For single pulse irradiation (Figure 3, SPI and $\Phi = 70 \mu\text{J}/\text{cm}^2$ the material is only partially structured, particularly craters are formed on the surface, while traces of LIPSS are present around the crater. For $\Phi = 75 \mu\text{J}/\text{cm}^2$ craters densify in a random way on the surface, their size is in the order of $1 \mu\text{m}$ and the areas among them is covered with inhomogeneous and pale LIPSS. For $\Phi = 80 \mu\text{J}/\text{cm}^2$ craters densify further and merge, while LIPSS appear to be less prominent compared to $\Phi = 75 \mu\text{J}/\text{cm}^2$. For higher fluences ($\Phi = 90 - 100 \mu\text{J}/\text{cm}^2$) the craters grow in number and size leading to film damage.

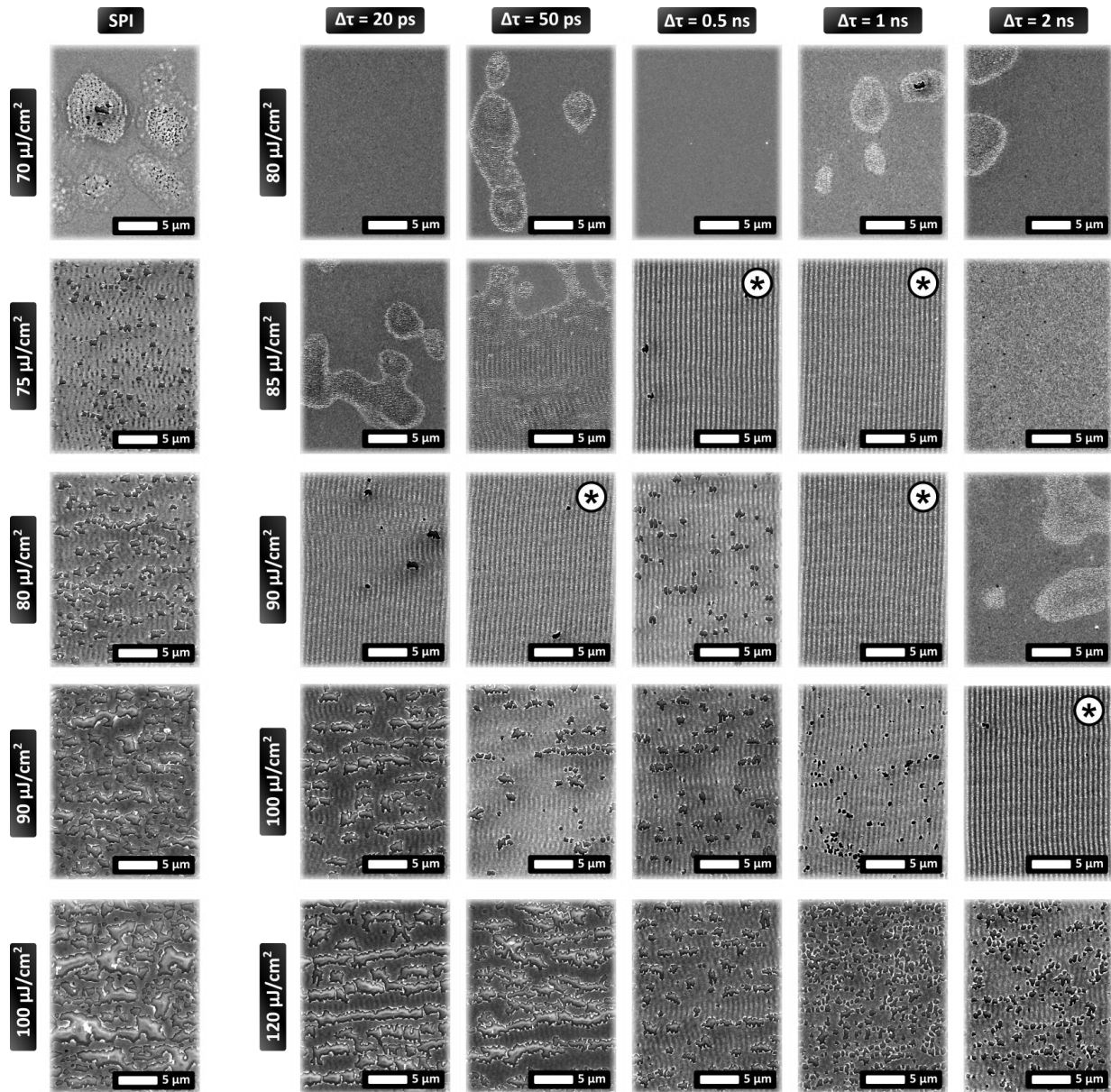


Figure 3 SEM images showing the different morphologies obtained by SPI and DPI at different fluences, Φ , and interpulse delays, $\Delta\tau$. Homogeneous and prominent LIPSS marked by '*'.

For double pulse irradiation (DPI), and $\Delta\tau = 20$ ps a different evolution of structures is observed upon increasing the fluence. For $\Phi = 80 \mu\text{J}/\text{cm}^2$ no trace of surface modification is observed, while for $\Phi = 85 \mu\text{J}/\text{cm}^2$ areas with nano roughness appear on the surface. Notably, for $\Phi = 90 \mu\text{J}/\text{cm}^2$ prominent and homogeneous LIPSS are formed together with few craters. Upon increase of fluence to 100 and 120 $\mu\text{J}/\text{cm}^2$, craters densify, grow and merge in a similar way as for SPI leading to surface damage.

The same trend is observed in all the cases of DPI presented in Figure 3; At low Φ values, random areas with nano roughness appear on the surface. At intermediate Φ values, homogeneous LIPSS are formed on the surface for most of the interpulse delays examined. As Φ takes higher values, craters are formed, densify, grow, and damage the surface. The specific fluence threshold leading to the formation of the

morphologies varies depending on the interpulse delay. Homogeneous and prominent LIPSS, marked by '*' in Figure 3, are formed almost in all cases of DPI; in particular, for $\Delta\tau = 50$ ps LIPSS are formed at $\Phi = 90 \mu\text{J}/\text{cm}^2$, for $\Delta\tau = 0.5$ ns at $\Phi = 85 \mu\text{J}/\text{cm}^2$, for $\Delta\tau = 1$ ns at $\Phi = 85$ & $90 \mu\text{J}/\text{cm}^2$ and finally for $\Delta\tau = 2$ ns at $\Phi = 100 \mu\text{J}/\text{cm}^2$. The observed variation of the Φ values leading to optimum LIPSS structures is attributed to the ultrafast dynamics affected by the interpulse delay. Nevertheless, a deep understanding of the underlying mechanisms needs to be further studied and theoretically investigated.

b) LIPSS Process window in respect to the $\Delta\tau$ value

The pulse-to-pulse overlap has a similar impact as Φ to LIPSS formation. Therefore, different combinations of Φ and O_v lead to homogeneous LIPSS formation, as presented in Figure 4. In this figure, each type of morphology is indicated with a specific color. In particular, combination of process parameters that led to non-textured surface are indicated with white. Transition regimes, in which we have a partial development of LIPSS, but some areas stay non-textured, are marked by pale yellow. Areas that have been textured homogeneously with LIPSS without craters (less than 5 craters with diameter larger than 500 nm within an area of $500\mu\text{m}^2$) are marked with yellow. Areas that show significant formation of craters are marked with brown, while damaged areas are marked with grey. Another type of morphology observed, marked with pink, indicates areas consisting of the generation of LIPSS with two different periods formed at the same irradiation conditions. This type of morphology will be discussed in detail in the following section e).

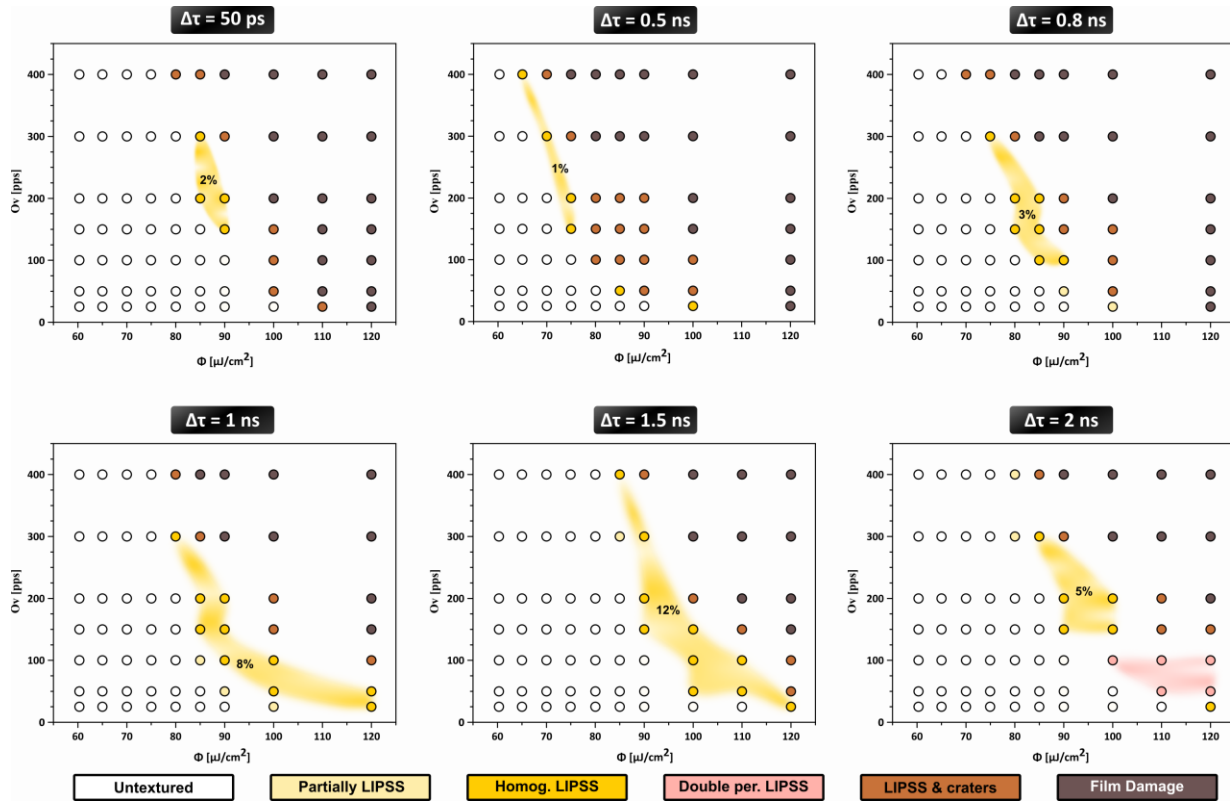


Figure 4 Graphs showing the resulting morphology upon systematic variation of two process parameters (Φ & Ov) for six interpulse delay ($\Delta\tau$) values. The colour of the symbols corresponds to the different morphology attained for each set of parameters as indicated in the legend shown at the bottom. The yellow areas marked in each graph indicate the range of process parameters that lead to homogeneous LIPSS formation. The percentages indicated correspond to the percentage of the process parameters providing homogeneous LIPSS, with respect to the whole investigated process window.

Following a careful examination of the graphs illustrated in Figure 4, it is evident that for a given $\Delta\tau$, there is interdependence between Φ and Ov values leading to homogeneous LIPSS formation. In particular, homogeneous LIPSS are formed for low fluence values combined with high pulse overlap, average fluence values and pulse overlap, as well as high fluence values with low pulse overlap. Interestingly, the average dose, D , is substantially different in each case and increases upon fluence decrease, from $D = 2 \text{ mJ/cm}^2$ when $\Phi = 100 \text{ } \mu\text{J/cm}^2$ to $D = 26 \text{ mJ/cm}^2$ when $\Phi = 65 \text{ } \mu\text{J/cm}^2$. Such D value variation for more than one order of magnitude points out that LIPSS formation occurs above a certain Φ threshold. When Φ is low ($\Phi = 65 \text{ } \mu\text{J/cm}^2$), that threshold is reached at a smaller spot radius and a large number of pulses is required to texture the area ($Ov = 400 \text{ pps}$). When the fluence is high ($\Phi = 100 \text{ } \mu\text{J/cm}^2$), the effective spot radius is larger and a small number of pulses is required to texture the area ($Ov = 20 \text{ pps}$). Thus, relatively higher Φ values are more effective for LIPSS formation and this is the trend observed for any $\Delta\tau$ value tested.

The effectiveness of the laser structuring process is indicated by the range of Ov and Φ values leading to homogeneous LIPSS generation. In order to have a qualitative representation of the process window range leading to homogeneous LIPSS generation, we mark the areas, A_{PW} , among symbols leading to homogeneous LIPSS with pale yellow color (Figure 4). Interestingly A_{PW} varies notably among the different $\Delta\tau$ tested, while A_{PW} is maximized at an optimum $\Delta\tau$ range $1 \text{ ns} < \Delta\tau < 1.5 \text{ ns}$. Theoretical investigations

indicate that at $t \sim 1$ ns after irradiation, for the fluence values considered here, the material's surface is still melted³², and microfluidic motion takes place on the molten surface⁴⁰. Moreover, it is expected that the molten material has acquired sufficient velocity, driven by the induced temperature gradients. Therefore, we hypothesize that microfluidic phenomena such as Marangoni instabilities and convection flow are playing key role in LIPSS formation. This hypothesis should be further investigated theoretically for the particular conditions considered here.

c) Early stages of LIPSS formation and the appearance of craters

The first stages of structure formation provide significant findings on underlining the different response of the material upon SPI and DPI respectively. To analyse the initial stages we illustrate in Figure 5 SEM images comparing an unprocessed area with the surfaces processed with single and double pulses at different irradiation doses for $\Delta\tau = 1$ ns.

In the unprocessed area shown on Figure 5, i), some imperfections occurred during film deposition are evident, with a characteristic size in the order of 300 nm. We consider that such imperfections may act as hot spots and locally amplify the intensity of the incident laser field⁵². Upon SPI with $\Phi = 70 \mu\text{J}/\text{cm}^2$ and $Ov = 50$ pps (Figure 5, ii, SPI) a number of craters appear on the surface together with a few faded traces of periodic structures surrounding them. Upon increase of dose, when $Ov = 100$ pps, areas covered by craters in close proximity are observed with traces of pale LIPSS surrounding the craters. Imperfections can be rarely found at that stage. This is suggesting that the initial ones present in the unprocessed surface have potentially evolved into craters due to electromagnetic field amplification in their proximity. When $Ov = 150$ pps the number of craters is significantly increased and LIPSS surrounding them become more prominent. At the same time LIPSS of adjacent craters become to overlap, giving rise to formation of inhomogeneous LIPSS areas (cyan frame in Figure 5, ii, SPI, $Ov = 150$ pps). The observed LIPSS distortion can be attributed to the random distribution of the craters; as a result, the inter-crater distance is not always an integer multiple of the SP wavelength giving rise to destructive interference.

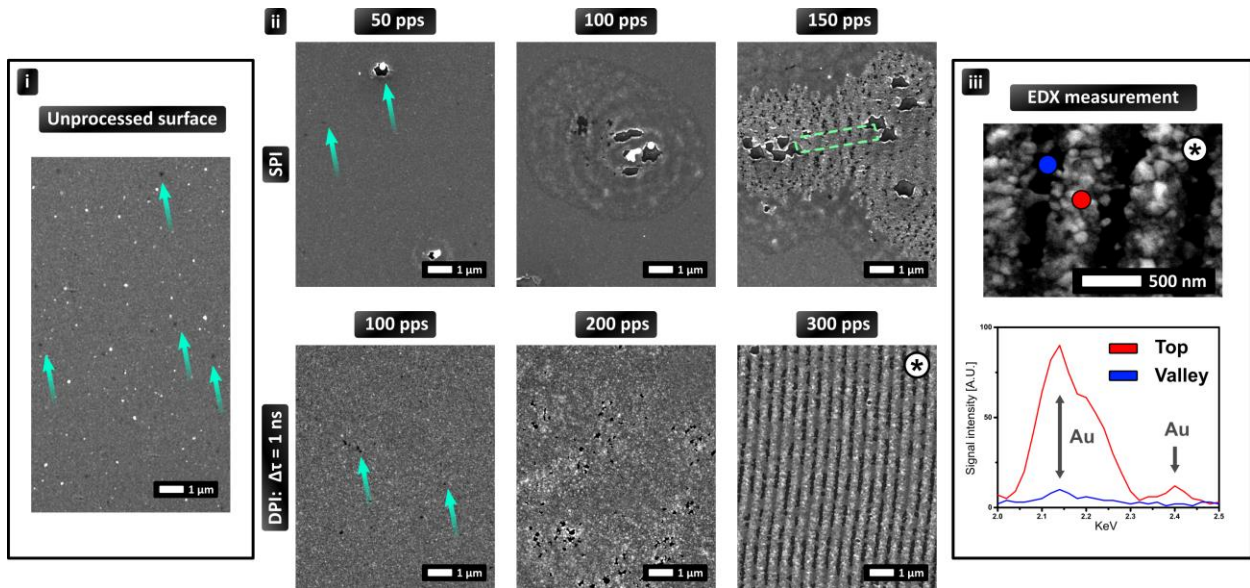


Figure 5 Comparison of the early stages of structure formation in the case of SPI and DPI respectively. i. Defects on unprocessed surface. ii. Structure appearance upon dose increase for SPI and DPI with $\Delta\tau = 1$ ns respectively. Fluence is $\Phi = 80 \text{ mJ}/\text{cm}^2$ for DPI and $\Phi = 70 \text{ mJ}/\text{cm}^2$ for SPI.

The first stages of structures formation in the DPI case was studied for $\Delta\tau = 1$ ns, as it lies within the optimum $\Delta\tau$ range ($0.8 \text{ ns} < \Delta\tau < 1.5 \text{ ns}$) for regular LIPSS formation. The corresponding SEM images shown in Figure 5, ii illustrate that for an initial O_v of 100 pps more imperfections are generated on the irradiated surface that maintain the same size compared to those present in the unprocessed one. For $O_v = 200$ pps the surface becomes roughened and the number of imperfections increases, whilst their size seem to grow slightly. Finally when $O_v = 300$ pps regular LIPSS cover the hole irradiated area, while no imperfections are observed. EDX measurements confirmed the entire removal of the film material in the areas between LIPSS (Figure 5, iii).

Conclusively, for SPI, craters precede LIPSS formation, setting the centers of electromagnetic interactions in a spatially incoherent way. That prevents the homogeneous LIPSS formation. For DPI the surface is progressively roughened, and the number of defects increases upon increase of the dose, without the formation of craters. In this case, LIPSS are formed prior to crater formation and as a result their spatial coherence is maintained. It is quite likely that the mechanism of LIPSS formation is different between the two cases; in particular, LIPSS in SPI are only formed due to film imperfections, whilst in DPI due to a laser-induced surface roughening effect.

d) LIPSS characteristics upon single and double pulse irradiation

In Figure 6, the optimum morphology obtained for the SPI or DPI cases is presented. In the case of single pulses (Figure 6, a) several defects are formed on the surface together with LIPSS, which cover partially the irradiated area. For DPI at $\Delta\tau = 1$ ns, homogenous and defect-free LIPSS areas are formed (Figure 6, a'). FT analysis shows that for single pulses (Figure 6, b), LIPSS are spatially incoherent, indicating that the textures cannot sustain sharp plasmonic resonances. Two characteristic periods are noted, namely $\Lambda_i = 648 \pm 1$ nm and $\Lambda_{ii} = 1000 \pm 2$ nm, with a relative magnitude of $\sim 3/4$ and $\sim 1/4$ respectively. Theoretical investigation carried out, identifies those periodicities as a result of SP excitation in the Au-substrate and air-Au interfaces respectively and will be discussed in paragraph e. In the case of $\Delta\tau = 1$ ns (Figure 6, b'), on the other hand, LIPSS are spatially coherent, with a single period of $\Lambda_i = 648 \pm 0.4$ nm. In both cases the LIPSS period close to 650 nm, corresponding to SP excitation in the Au-substrate interface is the dominant (Figure 6, b & b').

SPI and DPI results differ also in the directionality of the structures. To quantify the angular dispersion of

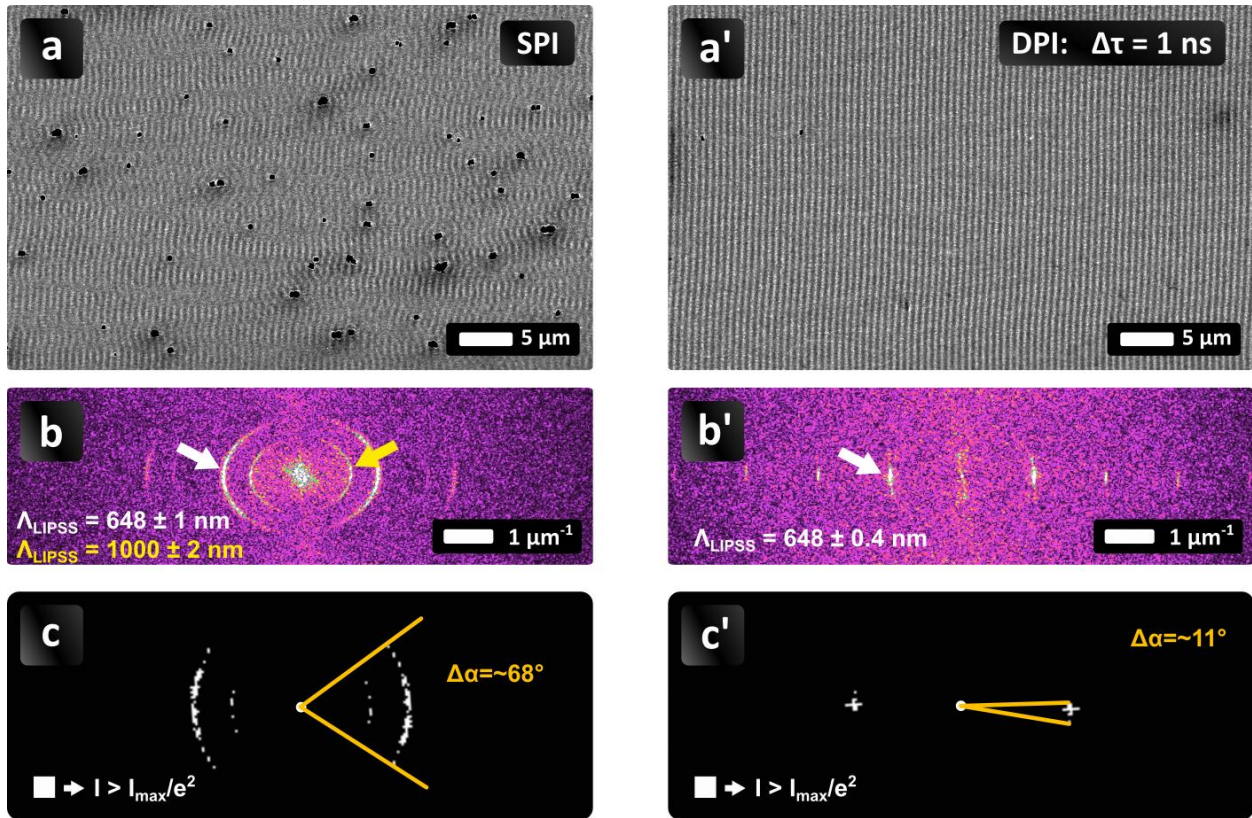


Figure 6 Comparison of optimized structures for SPI (a) and DPI (a') respectively. For SPI, $\Phi = 90 \mu\text{J}/\text{cm}^2$ and $Ov = 100 \text{ pps}$ whilst for DPI, $\Phi = 85 \mu\text{J}/\text{cm}^2$ and $Ov = 150 \text{ pps}$. Fourier transform (FT) maps are shown for SPI and DPI respectively in b and b'. An FT map showing the signal points with intensity $I > I_{\text{max}}/e^2$ are shown, in c and c', for SPI and DPI respectively.

the structures, the 2D - FT maps (Figure 6, b & b') was subjected to threshold analysis. A graph was produced in each case, showing in white the points exceeding the threshold of $1/e^2$ of maximum signal intensity in FT for $\Lambda \sim 640 \text{ nm}$. Based on the signal intensity, the angular dispersion of the structures can be estimated for SPI to $\Delta\alpha \sim 68^\circ$ (Figure 6, c) whereas in the case of DPI to $\Delta\alpha \sim 11^\circ$ (Figure 6, c').

e) HSFL and double period LIPSS

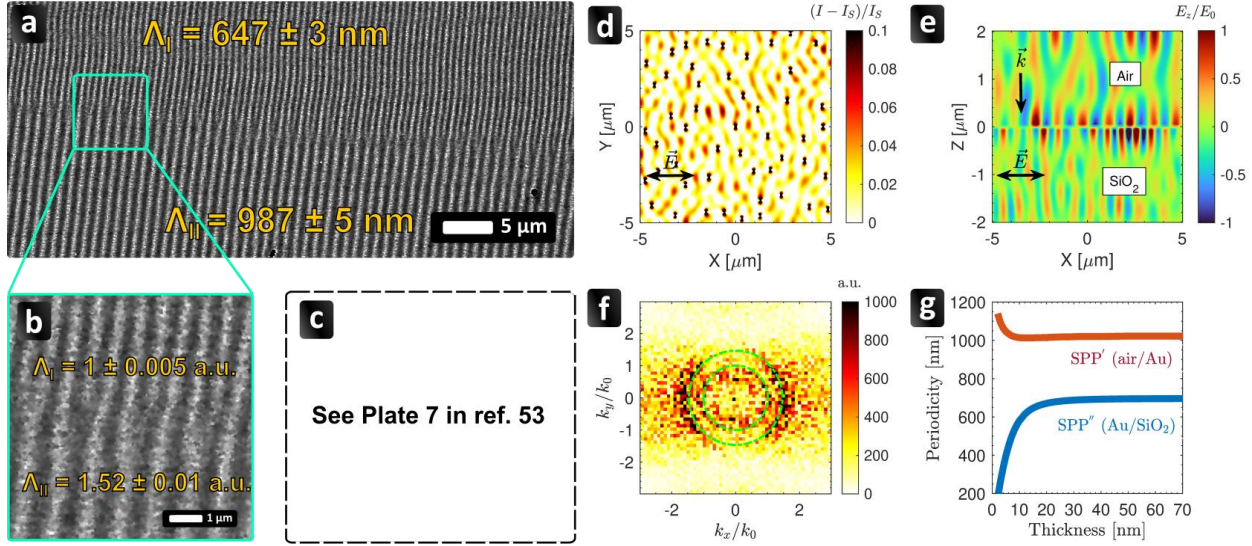


Figure 7 a,b) SEM image of Au surface processed with $\Delta t = 2$ ns, $N = 100$ pps, $\Phi = 100 \mu\text{J}/\text{cm}^2$. (c) Image of pinching instability of convection flow in silicon oil reproduced from ⁵³. (d) Intensity distribution in the xy (sample) plane below the top air/Au interface of a 32nm Au/SiO₂ thin film for $\lambda_L = 1026$ nm. (e) Absorbed energy distribution represented by the z -component of the electric field on the xz (propagation) plane of the air/Au film/dielectric system. SPPs are formed on both air/Au and Au/SiO₂ interfaces (around $Z=0$). The double-headed arrow indicates the orientation of the laser beam polarization. (f) Fourier spectrum of the intensity patterns in the xy plane showing quasi-periodic features of two distinct periodicities, $\Lambda_{top} \approx \lambda_L = 1026\text{nm}$ (inner circle $k_x/k_0 \approx 1$) and $\Lambda_{bottom} \approx 690\text{nm}$ (outer circle $k_x/k_0 \approx \lambda_L/\Lambda$). (g) Wavelengths of the two bound SPPs on air/Au/SiO₂ at $\lambda_L = 1026$ nm provided by the numerical solution of Eq.1. For the calculations, we used thickness independent Au permittivity taken from Ref. [12].

As discussed in the previous paragraphs, double period LIPSS (2P-LIPSS) are formed upon both SPI and DPI, nonetheless the homogeneity of the structures differs strikingly between the two cases. For SPI, double period LIPSS are observed sporadically for irradiation doses above the LIPSS formation threshold (see for example, Figure 6, a). For DPI and specifically when $\Delta t = 2$ ns, 2P-LIPSS are formed over extended areas. Notably, several neighboring combinations of Φ and N led to 2P-LIPSS, as indicated by pink area in Figure 4. Figure 7 a) and b) illustrates an example of 2P-LIPSS generation upon DPI, while the two periods measured are $\Lambda_I = 648 \pm 1$ nm and $\Lambda_{II} = 987 \pm 5$ nm.

The origin of the two LIPSS periods observed can be attributed to the SPP periods, excited at the Au-substrate and air-Au interfaces respectively. To account for the effect of such two coinciding electromagnetic modes on surface structuring, we employ the theoretical model described in paragraph II.b. Figure 7 d illustrates the energy absorption patterns in the transverse plane on Au film during irradiation, while Figure 7 f illustrates the corresponding Fast Fourier Transform (FFT) of the periodic features representative to the irradiation conditions described above. The presence of the nano-holes on the metallic surfaces favours strong energy confinement at their edges localized parallel to the laser polarization, On the contrary the far fields, consisting of SPPs and quasi-cylindrical wave components, exhibit maxima and minima that are formed perpendicularly to the laser polarization. As a result, the dominant periodic/quasi-periodic absorption patterns are observed with a periodicity of $\Lambda_{bottom} = 690$ nm (seen at $k_x/k_0 \approx \lambda_L/\Lambda$ at FFT). Furthermore, periodic features of periodicity close to the laser wavelength are also captured in FFT ($k_x/k_0 \approx 1$), which are attributed to the interference patterns created at the air/metal interface. The two periodicities observed are not only the result due to the interference of the incident beam with TM-polarized SPPs and quasi-cylindrical waves on air/metal

interface but also the film thickness is small enough to promote two supported SPPs which can be excited and couple each other simultaneously at the two interfaces of the thin film. In Figure 7, e we present a side view of the absorbed energy distribution along the thin film on the xz plane where the z -component of the electric field is normalized by its maximum value. We observe that the SPPs confined to the air/metal as well as at the metal/glass interfaces propagate along the x -axis with evanescent decay in the perpendicular z -direction. The periodicity of the SPP developed at the air/metal interface is nearly equal to the laser wavelength ($\Lambda_{top} = 1026$ nm) while the SPP at the metal/glass interface is nearly equal to $\lambda_L/n_g \approx 690$ nm where $n_g = \sqrt{\epsilon_g}$. This is an indication that LIPSS on Au thin films originate from coupled SPPs excited on both interfaces with periodicity expected very close to the SPP developed at the metal/glass interface. The two periods ($\Lambda_{bottom} = 690$ nm, $\Lambda_{top} = 1026$ nm) are very close to the experimental values ($\Lambda_I = 648 \pm 1$ nm and $\Lambda_{II} = 987 \pm 5$ nm).

The two SPP periodicities can also be predicted by applying the Maxwell equations at the interfaces of a three-layer (dielectric/metal/dielectric) system in order to determine the spatial field profile and dispersion of propagating waves for guided electromagnetic modes in waveguides. If the metallic medium is thin enough compared to the penetration depth, such a system is capable to support coupled SPP modes whose properties can be controlled by the thickness of the metallic film. This can be clearly seen in the dispersion relation of flat thin films in an asymmetric dielectric environment [6]

$$\exp(-2k_m d) = \frac{k_m/\epsilon_m + k_a/\epsilon_a}{k_m/\epsilon_m - k_a/\epsilon_a} \cdot \frac{k_m/\epsilon_m + k_g/\epsilon_g}{k_m/\epsilon_m - k_g/\epsilon_g} \quad (1)$$

Where

$$k_j = \pm \sqrt{\beta^2 - \epsilon_j k_0^2} \quad (2)$$

In Eq. (1), $j = a, m$ or g denotes the three media (a for air, g for glass, m for metal), d is the thickness of the film, β is the propagation constant of the SPP, and $k_0 = 2\pi/\lambda_L$ is the free-space wavenumber at the laser wavelength. The numerical solution of Eq. provides the supported SPP wavelength $\Lambda = 2\pi/Re(\beta)$ for given film thickness. The calculated wavelengths of the two-interface surface plasmons are dependent on the film thickness, as illustrated in Figure 7, g. Each interface can sustain bound SPPs. With increasing the film thickness to $d > 35$ nm, the SPPs at the two interfaces become decoupled and separated while strong coupling occurs as the thickness decreases below ~ 30 nm, while the SPP periodicity decreases abruptly from 687 nm to 395 nm at $d = 5$ nm for the lower SPP mode. For $d = 32$ nm the SPP periodicity is $\Lambda = 700$ nm (Figure 7, f, green dot line) which are very close to the captured periodicity of the energy absorption patterns found by simulation. Both theoretical values are quite close the experimentally observed periods validating their electromagnetic origin.

The underlining mechanism permitting the coexistence of homogeneous 2P-LIPSS should be sought in the contribution of hydrodynamics (Process II). [47] In Figure 7, b, a part of the processed surface is shown in detail, demonstrating the transition area between the two different LIPSS periods. The obtained LIPSS pattern resembles in detail a type of convection flow identified as “pinching Instability” shown in Figure 7, c, reproduced from ⁵³. In order to facilitate the comparison of the periods between Figure 7, b and c, the two LIPSS periods on Au are normalized in accordance to the smaller value giving $\Lambda'_I = 1 \pm 0.005$ a.u and $\Lambda'_{II} = 1.52 \pm 0.01$ a.u. The corresponding two periods, estimated in Figure 7, c are $\Lambda'_I = 1 \pm 0.02$ a.u and $\Lambda'_{II} = 1.48 \pm 0.02$ a.u. Even though the values do not match within the error limits their relative difference is $\sim 2.5\%$ pointing out that convection flow could potentially play a role in the formation of 2P- LIPSS over large areas. Significant similarities between the obtained structures and convection flow patterns have been also reported on steel upon DPI ¹⁴ and theoretical works¹⁹³³ describe the important contribution of Marangoni instability and convection flow to LIPSS formation. According to such theoretical works, the instability pattern strongly depends on the local excitation conditions. In this context we hypothesize that a periodic heat distribution on the melted material can impose a double period, which can hydrodynamically coexist only upon DPI due to convection flow. Therefore, the 2P-LIPSS formation can be considered as the result of the synergistic effect of SPPs with two periods that drives the generation of a pinching hydrodynamic instability.

f) Ellipsometric measurements

A SEM image of one of the fabricated nanostructures, tested by spectroscopic ellipsometry, is shown in Figure 8, a. The grain size of deposited thin Au film reaches up to 20-25 nm. The ripple period estimated in this image is $\Lambda = 620 \pm 10$ nm. Typical ellipsometric angles spectra of a patterned thin Au film are shown in Figure 8b,c. We recorded a pair of ellipsometric parameters, Ψ and Δ in the wavelength range from 250 nm to 1000 nm as a function of angle of incidence. Quite unexpectedly, we found that the fabricated nanostructures demonstrate topological darkness in reflection at some wavelength and an angle of light incidence. Figure 8b shows the ellipsometric reflection measured at three different angles of incidence for the sample shown in Figure 8a. We see that the polarized p-reflection goes to zero at an angle of around 62° and wavelength of ~ 592 nm. At the condition of zero reflection, the phase of light Δ exhibits 180° -jump behaviour which is a tell-tale feature of topological darkness ⁵⁴ (see Figs. 8e). The sharp phase variations and the deep minimum of Ψ for the p-polarized reflection (the red line in Figs. 8 b) quickly disappear when the incident angle is changed ever so slightly (by several degrees). It is worth noting that both Ψ and Δ demonstrate complicated behaviour due to diffraction of incident light on the periodic structure as well as due to light scattering connected with the imperfection of fabricated nanostructures.

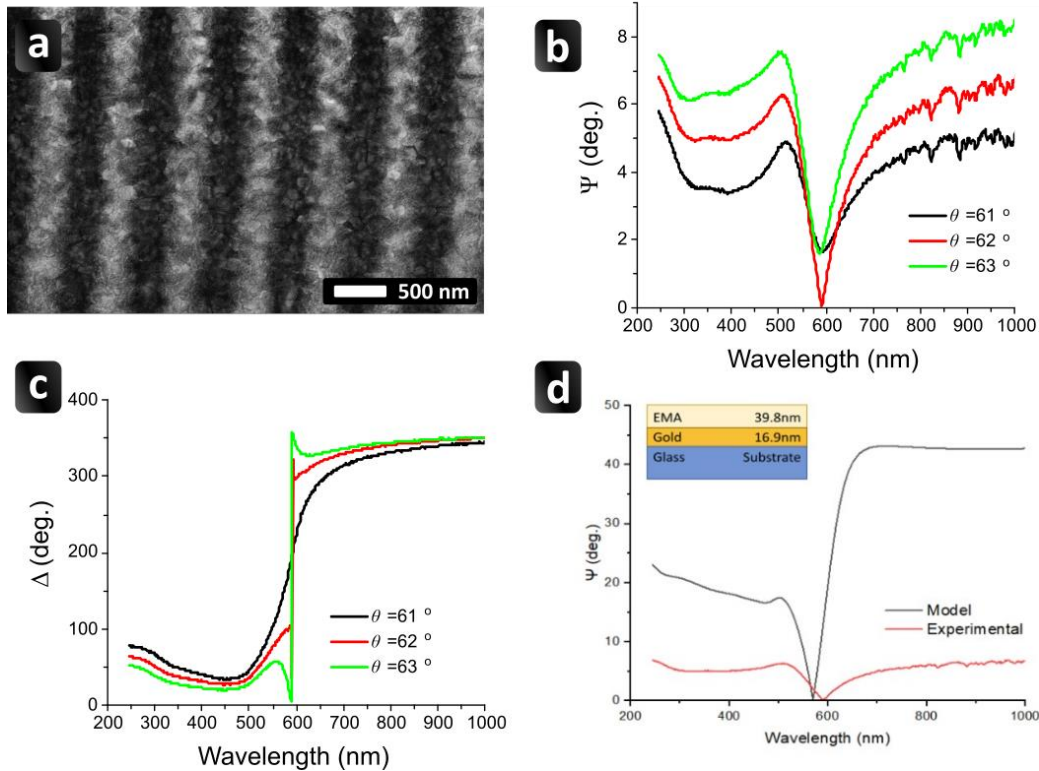


Figure 8 (a) High resolution SEM images of one of the fabricated LIPSS nanostructures. (b) Measured changes of ellipsometric parameter Ψ (amplitude) as a function of the incident wavelengths and angles for the LIPSS nanostructures shown in (a). The reflection exhibits total darkness at the angle of incidence of 62° and wavelength of ~ 590 nm. (c) Measured changes of ellipsometric parameter Δ (phase) as a function of the incident wavelengths and angles for the LIPSS nanostructures shown in (a). (d) Comparison of the experimental and modelled ellipsometric parameters Ψ for angle of incidence of 62° for the the LIPSS nanostructures shown in (a).

To model the measured optical spectra, we applied the effective-medium approximation⁵⁵ for the top metal layer of LIPSS and the Fresnel theory for the whole sample. The system geometry was set up according to the SEM data of the samples (see Figure 8a). The modelling results for the geometry of Figure 8a are shown in Figure 8d (along with modelling geometry shown in the inset), where they are compared with the experimental data. It can be observed that the theory reproduces well the position of topological minima for the ellipsometric function of Ψ and the jump of Δ at the resonance, but the absolute values of Ψ outside of the resonance are much larger than those measured experimentally. This could be partly attributed to some limitation of the EMA model, though mainly to the light scattering due to structural imperfections in fabricated LIPSS which implies that we extended the concept of topological darkness to scattering media. Further work is in progress to address this matter.

g) Conclusions

The results discussed in this work demonstrate the possibility of generating plasmonic sensing elements on thin Au film upon laser irradiation. To this end, a systematic study of LIPSS formation on thin Au film upon single and double pulse irradiation is presented. The formation of highly regular LIPSS over large

areas on thin Au film surface upon double pulse irradiation is investigated, and the underlying formation mechanism is discussed. In particular, the key role of the interpulse delay in producing regular LIPSS structures over large areas is discussed and the optimum interpulse delay regime is identified to range between $\Delta\tau = 0.8$ ns and $\Delta\tau = 1.5$ ns. The striking differences in the outcome of single and double pulse processing underline the hydrodynamic origin behind the regularity of LIPSS formation. Electromagnetic simulation of the propagation of the incident laser beam on Au surface provides insight on the origin of LIPSS periods in very good agreement with the experimental data. Furthermore, ellipsometry measurements validate the possibility of using the substrate as plasmonic sensor. Indeed, the reflection by the regular LIPSS areas exhibits a characteristic total darkness effect at the angle of incidence of 62° and the wavelength of ~ 590 nm. We believe that our results provide comprehensive and valuable data for the generation of functional periodic structures on Au thin layers and can further contribute to the development of new applications of laser functionalized surfaces.

Acknowledgements

This work was supported by the EU's H2020 framework programme for research and innovation under the NFFA-Europe-Pilot project (Grant No. 101007417). VGK and ANG acknowledge support of Graphene Flagship programme, Core 3 (881603).

Bibliography

- (1) Stratakis, E.; Bonse, J.; Heitz, J.; Siegel, J.; Tsihidis, G. D.; Skoulas, E.; Papadopoulos, A.; Mimidis, A.; Joel, A.-C.; Comanns, P.; Krüger, J.; Florian, C.; Fuentes-Edfuf, Y.; Solis, J.; Baumgartner, W. Laser Engineering of Biomimetic Surfaces. *Materials Science and Engineering: R: Reports* **2020**, *141* (May), 100562. <https://doi.org/10.1016/j.mser.2020.100562>.
- (2) Vorobyev, A. Y.; Guo, C. Colorizing Metals with Femtosecond Laser Pulses. *Appl Phys Lett* **2008**, *92*, 041914. <https://doi.org/10.1063/1.2834902>.
- (3) Zorba, V.; Stratakis, E.; Barberoglou, M.; Spanakis, E.; Tzanetakis, P.; Anastasiadis, S. H.; Fotakis, C. Biomimetic Artificial Surfaces Quantitatively Reproduce the Water Repellency of a Lotus Leaf. *Advanced Materials* **2008**, *20* (21), 4049–4054. <https://doi.org/10.1002/adma.200800651>.
- (4) Römer, G.; Cerro, D. A. del; Groenendijk, M. N. W.; Huis, A. J.; Sipkema, R. C. J. Ultra Short Pulse Laser Generated Surface Textures for Anti-Ice Applications in Aviation. *29th International Congress on Applications of Lasers and Electro-Optics, ICALEO* **2010**, 1356–1360.
- (5) Papadopoulos, A.; Skoulas, E.; Mimidis, A.; Perrakis, G.; Kenanakis, G.; Tsihidis, G. D.; Stratakis, E. Biomimetic Omnidirectional Antireflective Glass via Direct Ultrafast Laser Nanostructuring. *Advanced Materials* **2019**, *1901123*, 1901123. <https://doi.org/10.1002/adma.201901123>.
- (6) Skoulas, E.; Mimidis, A.; Demeridou, I.; Tsihidis, G. D.; Stratakis, E. *Polarization Dependent Spike Formation on Black Silicon via Ultrafast Laser Structuring*; Vol. 22.

- (7) Lutey, A. H. A.; Gemini, L.; Romoli, L.; Lazzini, G.; Fuso, F.; Faucon, M.; Kling, R. Towards Laser-Textured Antibacterial Surfaces. *Sci Rep* **2018**, *8* (1), 10112. <https://doi.org/10.1038/s41598-018-28454-2>.
- (8) Vlahou, M.; Fraggelakis, F.; Manganas, P.; Tsibidis, G. D.; Ranella, A.; Stratakis, E. Fabrication of Biomimetic 2D Nanostructures through Irradiation of Stainless Steel Surfaces with Double Femtosecond Pulses. *Nanomaterials* **2022**, *12* (4), 2079–4991. <https://doi.org/10.3390/nano12040623>.
- (9) Kabashin, A. v.; Evans, P.; Pastkovsky, S.; Hendren, W.; Wurtz, G. A.; Atkinson, R.; Pollard, R.; Podolskiy, V. A.; Zayats, A. v. Plasmonic Nanorod Metamaterials for Biosensing. *Nat Mater* **2009**, *8* (11), 867–871. <https://doi.org/10.1038/nmat2546>.
- (10) Skoulas, E.; Tasolamprou, A. C.; Kenanakis, G.; Stratakis, E. Laser Induced Periodic Surface Structures as Polarizing Optical Elements. *Appl Surf Sci* **2021**, *541* (November 2020), 148470. <https://doi.org/10.1016/j.apsusc.2020.148470>.
- (11) C.C. Tang; Y. Bando; T. Sato; K. Kurashima. Uniform Boron Nitride Coatings on Silicon Carbide Nanowires. *Advanced Materials* **2002**, *14* (15), 1046–1049.
- (12) Elbourne, A.; Crawford, R. J.; Ivanova, E. P. Nano-Structured Antimicrobial Surfaces: From Nature to Synthetic Analogues. *J Colloid Interface Sci* **2017**, *508*, 603–616. <https://doi.org/10.1016/j.jcis.2017.07.021>.
- (13) Müller, F. A.; Kunz, C.; Gräf, S. Bio-Inspired Functional Surfaces Based on Laser-Induced Periodic Surface Structures. *Materials* **2016**, *9* (6). <https://doi.org/10.3390/ma9060476>.
- (14) Fraggelakis, F.; Mincuzzi, G.; Lopez, J.; Manek-Hönninger, I.; Kling, R. Controlling 2D Laser Nano Structuring over Large Area with Double Femtosecond Pulses. *Appl Surf Sci* **2019**, *470*, 677–686. <https://doi.org/https://doi.org/10.1016/j.apsusc.2018.11.106>.
- (15) Cong, J.; Yang, J.; Zhao, B.; Xu, X. Fabricating Subwavelength Dot-Matrix Surface Structures of Molybdenum by Transient Correlated Actions of Two-Color Femtosecond Laser Beams. *Opt Express* **2015**, *23* (4), 5357. <https://doi.org/10.1364/OE.23.005357>.
- (16) Barberoglou, M.; Gray, D.; Magoulakis, E.; Fotakis, C.; Loukakos, P. a; Stratakis, E. Controlling Ripples' Periodicity Using Temporally Delayed Femtosecond Laser Double Pulses. *Opt Express* **2013**, *21* (15), 18501–18508. <https://doi.org/10.1364/OE.21.018501>.
- (17) Bonse, J.; Hohm, S.; Kirner, S. v.; Rosenfeld, A.; Kruger, J. Laser-Induced Periodic Surface Structures— A Scientific Evergreen. *IEEE Journal of Selected Topics in Quantum Electronics* **2017**, *23* (3), 9000615. <https://doi.org/10.1109/JSTQE.2016.2614183>.
- (18) Nathala, C. S. R.; Ajami, A.; Ionin, A. A.; Kudryashov, S. I.; Makarov, S. v; Ganz, T.; Assion, A.; Husinsky, W. Experimental Study of Fs-Laser Induced Sub-100-Nm Periodic Surface Structures on Titanium. *Opt Express* **2015**, *23* (5), 5915. <https://doi.org/10.1364/oe.23.005915>.
- (19) Tsibidis, G. D.; Fotakis, C.; Stratakis, E. From Ripples to Spikes: A Hydrodynamical Mechanism to Interpret Femtosecond Laser-Induced Self-Assembled Structures. *Phys Rev B* **2015**, *92* (4), 041405. <https://doi.org/10.1103/PhysRevB.92.041405>.

- (20) Romano, J.-M.; Garcia-Giron, A.; Penchev, P.; Dimov, S. Triangular Laser-Induced Submicron Textures for Functionalising Stainless Steel Surfaces. *Appl Surf Sci* **2018**, *440*, 162–169. <https://doi.org/10.1016/j.apsusc.2018.01.086>.
- (21) Skoulas, E.; Manousaki, A.; Fotakis, C.; Stratakis, E. Biomimetic Surface Structuring Using Cylindrical Vector Femtosecond Laser Beams. *Sci Rep* **2017**, *7* (1), 45114. <https://doi.org/10.1038/srep45114>.
- (22) Bonse, J.; Gräf, S. Maxwell Meets Marangoni—A Review of Theories on Laser-Induced Periodic Surface Structures. *Laser Photon Rev* **2020**, *2000215*, 1–25. <https://doi.org/10.1002/lpor.202000215>.
- (23) Skolski, J. Z. P.; Römer, G. R. B. E.; Obona, J. v; Ocelik, V.; Huis, A. J.; Hosson, J. T. M. de. Inhomogeneous Absorption of Laser Radiation: Trigger of LIPSS Formation. *Journal of Laser Micro/Nanoengineering* **2013**, *8* (1), 1–5. <https://doi.org/10.2961/jlmn.2013.01.0001>.
- (24) Sokolowski-Tinten, K.; Bonse, J.; Barty, A.; Chapman, H. N.; Bajt, S.; Bogan, M. J.; Boutet, S.; Cavalleri, A.; Dusterer, S.; Frank, M.; Hajdu, J.; Hau-Riege, S.; Marchesini, S.; Stojanovic, N.; Treusch, R. In-Situ Observation of the Formation of Laser-Induced Periodic Surface Structures with Extreme Spatial and Temporal Resolution. **2022**, 1–26.
- (25) Garcia-Lechuga, M.; Puerto, D.; Fuentes-Edfuf, Y.; Solis, J.; Siegel, J. Ultrafast Moving-Spot Microscopy: Birth and Growth of Laser-Induced Periodic Surface Structures. *ACS Photonics* **2016**, *3* (10), 1961–1967. <https://doi.org/10.1021/acsp Photonics.6b00514>.
- (26) Sedao, X.; Abou Saleh, A.; Rudenko, A.; Douillard, T.; Esnouf, C.; Reynaud, S.; Maurice, C.; Pigeon, F.; Garrelie, F.; Colombier, J. P. Self-Arranged Periodic Nanovoids by Ultrafast Laser-Induced Near-Field Enhancement. *ACS Photonics* **2018**, *5* (4), 1418–1426. <https://doi.org/10.1021/acsp Photonics.7b01438>.
- (27) Tsibidis, G. D.; Barberoglou, M.; Loukakos, P. A.; Stratakis, E.; Fotakis, C. Dynamics of Ripple Formation on Silicon Surfaces by Ultrashort Laser Pulses in Subablation Conditions. *Phys Rev B* **2012**, *86* (11), 115316. <https://doi.org/10.1103/PhysRevB.86.115316>.
- (28) Derrien, T. J. Y. Y.; Itina, T. E.; Torres, R.; Sarnet, T.; Sentis, M. Possible Surface Plasmon Polariton Excitation under Femtosecond Laser Irradiation of Silicon. *J Appl Phys* **2013**, *114* (8). <https://doi.org/10.1063/1.4818433>.
- (29) Rudenko, A.; Mauclair, C.; Garrelie, F.; Stoian, R.; Colombier, J. P. Light Absorption by Surface Nanoholes and Nanobumps. *Appl Surf Sci* **2019**, *470*, 228–233. <https://doi.org/10.1016/j.apsusc.2018.11.111>.
- (30) Zhang, H.; Colombier, J.; Li, C.; Faure, N.; Cheng, G.; Stoian, R. Coherence in Ultrafast Laser-Induced Periodic Surface Structures. *Phys Rev B* **2015**, *92*, 174109, 1–14. <https://doi.org/10.1103/PhysRevB.92.174109>.
- (31) Bonse, J.; Rosenfeld, A.; Krüger, J. On the Role of Surface Plasmon Polaritons in the Formation of Laser-Induced Periodic Surface Structures upon Irradiation of Silicon by Femtosecond-Laser Pulses. *J Appl Phys* **2009**, *106*, 104910. <https://doi.org/10.1063/1.3261734>.

- (32) Sedao, X.; Shugaev, M. v.; Wu, C.; Douillard, T.; Esnouf, C.; Maurice, C.; Reynaud, S.; Pigeon, F.; Garrelie, F.; Zhigilei, L. v.; Colombier, J. P. Growth Twinning and Generation of High-Frequency Surface Nanostructures in Ultrafast Laser-Induced Transient Melting and Resolidification. *ACS Nano* **2016**, *10* (7), 6995–7007. <https://doi.org/10.1021/acsnano.6b02970>.
- (33) Rudenko, A.; Abou-Saleh, A.; Pigeon, F.; Mauclair, C.; Garrelie, F.; Stoian, R.; Colombier, J. P. High-Frequency Periodic Patterns Driven by Non-Radiative Fields Coupled with Marangoni Convection Instabilities on Laser-Excited Metal Surfaces. *Acta Mater* **2020**, *194*, 93–105. <https://doi.org/10.1016/j.actamat.2020.04.058>.
- (34) Fraggelakis, F.; Giannuzzi, G.; Gaudio, C.; Manek-Hönninger, I.; Mincuzzi, G.; Ancona, A.; Kling, R. Double- and Multi-Femtosecond Pulses Produced by Birefringent Crystals for the Generation of 2D Laser-Induced Structures on a Stainless Steel Surface. *Materials* **2019**, *12* (8), 1257. <https://doi.org/10.3390/ma12081257>.
- (35) Zhang, Y.; Jiang, Q.; Cao, K.; Chen, T.; Cheng, K.; Zhang, S.; Feng, D.; Jia, T.; Sun, Z.; Qiu, J. Extremely Regular Periodic Surface Structures in a Large Area Efficiently Induced on Silicon by Temporally Shaped Femtosecond Laser. *Photonics Res* **2021**, *9* (5), 839. <https://doi.org/10.1364/prj.418937>.
- (36) Fraggelakis, F.; Mincuzzi, G.; Lopez, J.; Kling, R.; Manek-Hönninger, I. Controlling Micron and Submicron Scale Laser Induced Surface Structures on Stainless Steel with Industrial Femtosecond Lasers. *Journal of Laser Micro/Nanoengineering* **2018**, *13* (3), 206–210. <https://doi.org/10.2961/jlmn.2018.03.0010>.
- (37) Abou Saleh, A.; Rudenko, A.; Reynaud, S.; Pigeon, F.; Garrelie, F.; Colombier, J. P. Sub-100 Nm 2D Nanopatterning on a Large Scale by Ultrafast Laser Energy Regulation. *Nanoscale* **2020**, *12* (12), 6609–6616. <https://doi.org/10.1039/c9nr09625f>.
- (38) Nakhoul, A.; Maurice, C.; Faure, N.; Garrelie, F.; Pigeon, F.; Colombier, J.-P. Tailoring the Surface Morphology of Ni at the Nanometric Scale by Ultrashort Laser Pulses. *Applied Physics A* **2022**, *128* (10). <https://doi.org/10.1007/s00339-022-06046-2>.
- (39) Fraggelakis, F.; Tsibidis, G. D.; Stratakis, E. Tailoring Submicrometer Periodic Surface Structures via Ultrashort Pulsed Direct Laser Interference Patterning. *Phys Rev B* **2021**, *103* (5), 054105. <https://doi.org/10.1103/PhysRevB.103.054105>.
- (40) Fraggelakis, F.; Tsibidis, G. D.; Stratakis, E. Ultrashort Pulsed Laser Induced Complex Surface Structures Generated by Tailoring the Melt Hydrodynamics. *Opto-electronic Advances* **2022**, *5* (3), 210052. <https://doi.org/10.29026/oea.2022.210052>.
- (41) Tsibidis, G. D.; Mansour, D.; Stratakis, E. Damage Threshold Evaluation of Thin Metallic Films Exposed to Femtosecond Laser Pulses: The Role of Material Thickness. *Opt Laser Technol* **2022**, *156*. <https://doi.org/10.1016/j.optlastec.2022.108484>.
- (42) Xie, H.; Zhao, B.; Cheng, J.; Chamoli, S. K.; Zou, T.; Xin, W.; Yang, J. Super-Regular Femtosecond Laser Nanolithography Based on Dual-Interface Plasmons Coupling. *Nanophotonics* **2021**, *10* (15), 3831–3842. <https://doi.org/10.1515/nanoph-2021-0329>.

- (43) Dostovalov, A. v.; Derrien, T. J. Y.; Lizunov, S. A.; Přeučil, F.; Okotrub, K. A.; Mocek, T.; Korolkov, V. P.; Babin, S. A.; Bulgakova, N. M. LIPSS on Thin Metallic Films: New Insights from Multiplicity of Laser-Excited Electromagnetic Modes and Efficiency of Metal Oxidation. *Appl Surf Sci* **2019**, *491* (April), 650–658. <https://doi.org/10.1016/j.apsusc.2019.05.171>.
- (44) Wang, J.; Guo, C. Ultrafast Dynamics of Femtosecond Laser-Induced Periodic Surface Pattern Formation on Metals. *Appl Phys Lett* **2005**, *87* (25), 1–3. <https://doi.org/10.1063/1.2146067>.
- (45) Sipe, J. E.; Young, J. F.; Preston, J. S.; van Driel, H. M. Laser-Induced Periodic Surface Structure. I. Theory. *Phys Rev B* **1983**, *27* (2), 1141–1154. <https://doi.org/10.1103/PhysRevB.27.1141>.
- (46) Yee, K. Numerical Solution of Initial Boundary Value Problems Involving Maxwell's Equations in Isotropic Media. *IEEE Trans Antennas Propag* **1966**, *14* (3), 302–307. <https://doi.org/10.1109/TAP.1966.1138693>.
- (47) Clemens, M.; Weiland, T. *DISCRETE ELECTROMAGNETISM WITH THE FINITE INTEGRATION TECHNIQUE*; 2001; Vol. 32.
- (48) Johnson, P. B.; Christy, R. W. Optical Constants of the Noble Metals. *Phys Rev B* **1972**, *6* (12), 4370–4379. <https://doi.org/10.1103/PhysRevB.6.4370>.
- (49) Skolski, J. Z. P.; Römer, G. R. B. E.; Vincenc Obona, J.; Huis in 't Veld, A. J. Modeling Laser-Induced Periodic Surface Structures: Finite-Difference Time-Domain Feedback Simulations. *J Appl Phys* **2014**, *115* (10), 103102. <https://doi.org/10.1063/1.4867759>.
- (50) Rudenko, A.; Mauclair, C.; Garrelie, F.; Stoian, R.; Colombier, J. P. Self-Organization of Surfaces on the Nanoscale by Topography-Mediated Selection of Quasi-Cylindrical and Plasmonic Waves. *Nanophotonics* **2019**, *8* (3), 459–465. <https://doi.org/10.1515/nanoph-2018-0206>.
- (51) Höhm, S.; Rosenfeld, A.; Krüger, J.; Bonse, J. Area Dependence of Femtosecond Laser-Induced Periodic Surface Structures for Varying Band Gap Materials after Double Pulse Excitation. *Appl Surf Sci* **2013**, *278*, 7–12. <https://doi.org/10.1016/j.apsusc.2012.10.188>.
- (52) Obara, G.; Maeda, N.; Miyanishi, T.; Terakawa, M.; Nedyalkov, N. N.; Obara, M. Plasmonic and Mie Scattering Control of Far-Field Interference for Regular Ripple Formation on Various Material Substrates. *Opt Express* **2011**, *19* (20), 19093. <https://doi.org/10.1364/oe.19.019093>.
- (53) Busse, F. H.; Whitehead, J. A. Instabilities of Convection Rolls in a High Prandtl Number Fluid. *J Fluid Mech* **1971**, *47* (2), 305–320. <https://doi.org/10.1017/S0022112071001071>.
- (54) Malassis, L.; Massé, P.; Tréguer-Delapierre, M.; Mornet, S.; Weisbecker, P.; Barois, P.; Simovski, C. R.; Kravets, V. G.; Grigorenko, A. N. Topological Darkness in Self-Assembled Plasmonic Metamaterials. *Advanced Materials* **2014**, *26* (2), 324–330. <https://doi.org/10.1002/adma.201303426>.
- (55) Tuck C. Choy. *Effective Medium Theory*; Oxford: Clarendon Press, 1999.